Check for updates

Arrangement of the photoreceptor mosaic in a diabetic rat model imaged with multiphoton microscopy

JUAN M. BUENO,[1,*] **RICARDO CRUZ-CASTILLO,**[2] **MARCELINO AVILÉS-TRIGUEROS,**[3] **AND NAZARIO BAUTISTA-ELIVAR**[4]

[1]*Laboratorio de Óptica, Instituto Universitario de Investigación en Óptica y Nanofísica, Universidad de Murcia, Murcia, Spain*
[2]*Área Académica de Matemáticas y Física, Instituto de Ciencias Básicas e Ingeniería, Universidad Autónoma del Estado de Hidalgo, Hidalgo, Mexico*
[3]*Departamento de Oftalmología, Facultad de Medicina, Universidad de Murcia e Instituto Murciano de Investigación Biosanitaria Virgen de la Arrixaca, "Campus Mare Nostrum" de Excelencia International, Murcia, Spain*
[4]*Departamento de Ingeniería Eléctrica, Tecnológico Nacional de México, Instituto Tecnológico de Pachuca, Hidalgo, Mexico*
[*]*bueno@um.es*

Abstract: Diabetic retinopathy (DR) is defined as a microvascular pathology. However, some data have suggested that the retinal photoreceptors (PRs) might be important in the pathogenesis of this ocular disease. In this study the organization of the PRs in control and diabetic-induced rats was compared using multiphoton microscopy. The PR mosaic was imaged at different locations in non-stained retinas. The density of PRs was directly quantified from cell counting. The spatially resolved density presents a double-slope pattern (from the central retina towards the periphery) in both healthy and pathological samples, although the values for the latter were significantly lower all across the retina. Moreover, Voronoi analysis was performed to explore changes in PR topography. In control specimens a hexagonally packed structure was dominant. However, despite the non-controlled effects of the disease in retinal structures, this PR regularity was fairly maintained in diabetic retinas.

1. Introduction

The use of animal models is essential in the analysis, early detection and treatment of retinal pathologies such as glaucoma [1], diabetic retinopathy (DR) [2] and age-related macular degeneration [3]. These are also useful to explore myopia progression and emmetropization processes [4], as well as for the development of retinal imaging devices [5,6].

Understanding certain retinal pathologies often requires an accurate visualization of structural features and an appropriate evaluation of cellular distribution within high-resolution images. Two-photon excitation fluorescence (TPEF) is a nonlinear imaging technique providing sub-cellular resolution of non-stained biological tissues [7]. In 2004, Imanishi and collaborators [8] were the first to report TPEF images (i.e. autofluorescence) of the retinal pigment epithelium in the mouse. Since then, different authors have used this type of microscopy to analyze retinal tissues (fixed, fresh and living) of different animal models and humans.

In the chicken retina, TPEF signals have been reliable and efficient, providing images of the retinal ganglion cells and the photoreceptor (PR) layer [9], and useful to analyze changes in the morphology of myopic eyes [10]. Retinal cells have also been studied with this type of microscopy in other animal models, such as porcine, rat, mouse and frog [11–15]. Moreover, by combining ophthalmoscopy and TPEF signals, images from the retina of living nonhuman primates [16,17] and mice [18,19] have been successfully acquired.

In human retinas, intrinsic TPEF sources were obtained from every retinal layer, ranging from the retinal nerve fibers to the PR outer segments [20]. TPEF images of the retinal pigment epithelium [21] have also been explored with this technique, and used as a possible age-related macular degeneration diagnosis [22,23].

Although this imaging approach is useful to understand the arrangement of retinal cells, all those previous measurements were used exclusively in healthy samples. Ocular diseases modify retinal structures and cellular distribution in a non-controlled manner. These changes in the intrinsic organization might seriously compromise regular metabolic and optical functions. However, experiments combining TPEF microscopy and pathological retinas have not been found in the literature by these authors.

In particular, DR (or diabetic eye disease) is a pathology caused by complications of diabetes mellitus [24,25]. Worldwide, one-third of the people suffering from diabetes show signs of DR [26]. Although fundus imaging routine checks and ophthalmological management might be effective at early stages, this condition can lead to blindness if left untreated. The key cause of DR is the damage of the retinal blood vessel network due to high glucose levels (i.e. narrowing of the retinal capillaries associated with reduced retinal blood flow). Most efforts have been centered on explaining the DR visual dysfunction based on the vasculature itself. However, a number of studies suggest that the neural retina is also involved and might play an important role in the development of DR [27–31]. Despite this, the potential contribution of PRs (covering most of the retinal metabolic activity) to this pathology has been often overlooked.

At least two (not mutually exclusive) hypotheses explain how PRs might influence DR development: hypoxia and exudative stress [30]. It becomes apparent that retinal neurodegeneration occurs prior to DR retinal neovascularization [28]. However, whether retinal neuropathology and early vascular changes develop independently is still under discussion.

For years the rat has been shown as an appropriate model for retinal imaging and the analysis of DR [32–35]. However, most experiments used immunohistochemistry procedures and to the best of our knowledge, no studies on the rat retinal cell distribution (neither healthy nor pathological) using TPEF imaging techniques have been previously reported.

In this work, TPEF microscopy has been used to image unstained retinas from rats with induced DR, to analyze the density and spatial distribution of the PRs. These will be compared with that of a group of control (healthy) rat eyes. It is important to note that along this work the term PR refers to both cones and rods. Under the present experimental conditions, the proposed imaging procedure is not able to distinguish between both types of retinal cells.

2. Methods

2.1. Experimental system

A custom multiphoton microscope in a backward configuration was used to obtain images of the retinal PR layer in a DR rat model. The experimental setup is shown in Fig. 1. The imaging instrument combines a mode-locked Ti:Shappire laser system (760 nm, 76 MHz repetition rate), a scanning unit, a Z-motor, and a detection unit (photomultiplier tube, PMT). A spectral filter (longpass 435-700nm, FGL435; Thorlabs Inc., Newton, NJ) was used to isolate the TPEF signal coming from the sample under study. The entire system was computer-controlled through home-made LabView^{TM} software. Further details about this instrument can be found elsewhere [9].

2.2. Animal model and tissue preparation

Diabetes was induced in a set of male adult Wistar rats (N=8, weight=200 g) by means of a unique dose (75 mg/kg) of streptozotocin diluted in citrate buffer, administered via intraperitoneal injection to each animal. During six weeks the animals (both diabetic and control groups) were
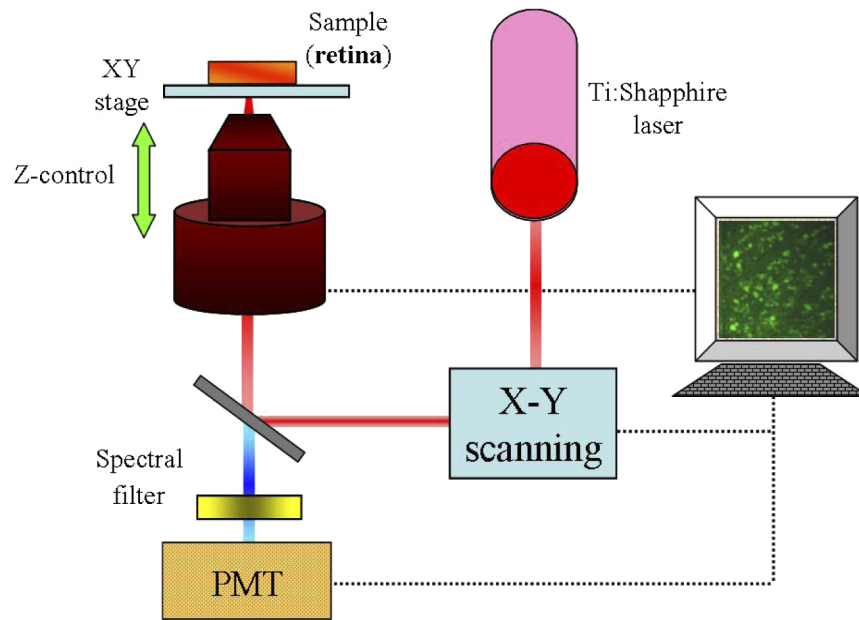
Fig. 1. Schematic diagram of the TPEF microscope (see text for details).

housed in a temperature and humidity controlled room, maintained on a 12-h light/dark cycle (lights on: 07:00-19:00 h) and having free access to food and water. At the end of that period blood glucose concentrations were monitored by means of an Assure II kit (MedWOW Ltd.). Blood was sampled from the tail just before a dark period. For all streptozotocin-injected animals, blood glucose levels were significantly higher (>200mg/dL) than those of the control group (N=5, <100 mg/dL). Animals were then sacrificed (by an overdose of sodium pentobarbital) and the ocular globes enucleated. Retinas were prepared as previously reported [36]. In brief, retinas were dissected and prepared as *in toto* whole-mount by making four radial cuts and fixated with a 4% paraformaldehyde solution in phosphate buffer (0.1 M; pH 7.2-7.4) for 2 hours at 4°C. The retinal tissue was flattened mounted with the vitreal side up on a microscope slide with a solution of 50% glycerol in 0.1 M sodium carbonate buffer (pH 9.0) as mounting media and covered with a 130-μm thick cover slip. None of the samples was stained. For the control group (without streptozocin injection) the protocol was similar. The entire experiment followed the guidelines of the Association for Research in Vision and Ophthalmology Statement for the Use of Animals in Ophthalmic and Vision Research.

2.3. Imaging and analysis procedures

Each non-stained retina was placed on the microscope stage for TPEF imaging. Four retinal quadrants were analyzed: superior-nasal (SN), superior-temporal (ST), inferior-nasal (IN), and inferior-temporal (IT). For each quadrant, TPEF images of the PR layer at different retinal eccentricities were acquired. These locations (named as #1, #2, #3, #4, and #5) were equidistant and placed along the radius from the optic nerve head towards the retinal periphery. The image size was 90×90 μm^2 (256×256 pixels). As a general idea, Fig. 2 presents the distribution of the imaged areas across the rat retina.

A simple visualization and a qualitative description of the TPEF retinal images do not provide accurate information on the cellular distribution and it is difficult to comment on or analyze the
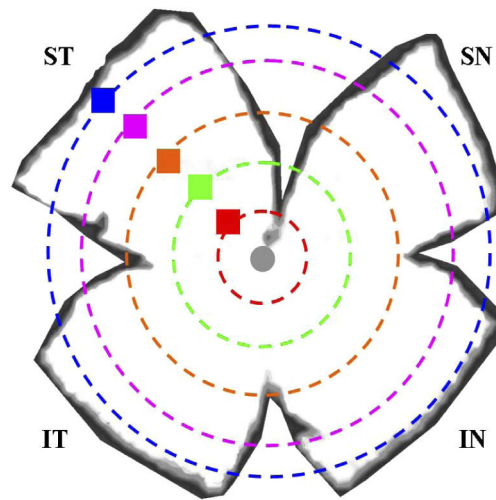
Fig. 2. Drawing depicting the location of the imaged areas with different retinal eccentricity. Only the areas in one of the four fields are represented. Locations are labeled in red (#1), green (#2), orange (#3), magenta (#4) and blue (#5).

changes suffered by pathological retinas. To provide objective data on this, the PR density was measured and the PR packing geometry was explored using Voronoi diagrams.

To compute the PR density we used the public domain image processing software "ImageJ". The procedure was similar to that described in [9,10]. For each image the visibility of the PRs was first enhanced using different filters. This included brightness-contrast adjusts, background subtraction and image contrast threshold. Then a binary process and a contrast inversion were also applied. Finally individual cells were manually tracked by the operator. Once the number of PRs across the entire image was known, the corresponding density was directly computed in cells/mm^2.

To validate the counting method, two different observers counted the number of PRs of 10 TPEF retinal images (5 from each group) in a blind masked fashion. Both, the sample and the retinal region within it were randomly chosen. Differences were always below 5%.

To further explore the spatial distribution of PRs and compare possible differences between the two groups of retinas, the packing structure was assessed using Voronoi tessellations [37]. These calculations and analyses were performed using custom Matlab^{TM} scripts. For this aim, the model of spatial location assumes individual cells small enough to be considered as mathematical points. This means that Voronoi polygons are not used to model neither the shape of the PRs nor their surrounding tissues. These points are used to establish the Voronoi tiling across the image as follows. Once the locations (i.e. XY coordinates) of all the individual PRs within an image are determined, this image is partitioned into polygons (i.e. Voronoi domains). Each polygon contains the area surrounding a particular PR that is closer to it than to any other PR. To avoid edge effects, only those polygons whose vertices all lie within the image under analysis are considered (i.e. Voronoi polygons at the edges of vessels and image borders were excluded).

Among the different parameters that can be obtained from Voronoi tessellations, two of them are used here: (i) the amount of polygons with a certain number of sides and (ii) the mean averaged distance among PRs. It is interesting to remember that the number of sides (or vertices) of a polygon is the same as the number of neighbours of a particular PR surrounded by that polygon.

When the image tiling is set, the coordinates of each PR (internal mathematical node of the Voronoi polygon) and their nearest neighbours are known. Thus, the distances d_i from each PR

to those neighbours can be computed. For every polygon, the mean averaged distance (D_{MA}) is defined as the ratio between the mean of the distances d_i and the number of neighbours (or polygon sides), n [38]. This measurement can be understood as a coefficient of expansion or contraction of the Voronoi polygon. In the present work, this represents a measure of the averaged space among neighboring PRs. That is, when comparing control and diabetic retinas, an increase in D_{MA} (i.e. an expansion) could be associated with a loss of PRs as result of the pathology.

The distribution of the number of sides of the Voronoi tiles gives an estimate of the type of packing and it is directly related to the regularity of the cellular arrangement. A perfect hexagonal array (i.e. all counted cells have six nearest neighbours) corresponds to the highest and ideal regularity. As a general rule, the higher the portion of hexagons across an image, the higher the regularity.

The statistical analysis was performed through the SPSS software. Differences were considered as significant when p<0.05. To check the normal distribution of the data the Kolmogorov-Smirnov test used. Paired Student's t-test was performed for normal distributions, otherwise the Mann-Whitney U test was employed.

3. Results

Although TPEF signals are able to visualize most retinal layers, from the nerve fiber layer to the retinal pigment epithelium [9,20], herein we are only interested in evaluating the PR spatial distributions in both control and diabetic rat retinas. Figure 3 presents illustrative TPEF images of different retinal structures (ganglion cells, inner nuclear, capillaries and PRs) acquired with our microscope. Different biological features are clearly visualized at a high spatial resolution. In particular, individual cells from both the ganglion cell layer and the PR mosaic can be observed. As already known [8,39], since the samples here used were unstained, this TPEF signal is exclusively due to autofluorescence (i.e. local endogenous fluorescence).
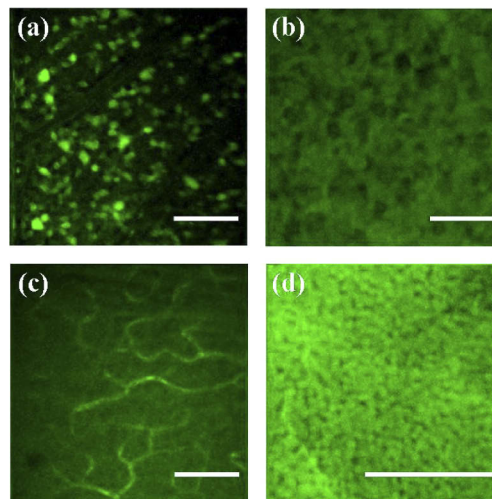

Fig. 3. TPEF microscopy images of different layers of the rat retina: retinal ganglion cells (a), inner nuclear (b), capillaries (c) and PRs (d). Scale bar: 50 µm.

The TPEF intensity profile as a function of depth is not constant across the retina (Fig. 4). Unlike the cornea, where a progressive decrease in signal appears with depth [40], for the retina this depends on the imaged retinal layer. It can be seen that this profile presents two local maxima corresponding to the PR mosaic and the retinal ganglion cell layer (as indicated). In particular, the signal at these two locations is ~16% above the averaged intensity. In addition, for the sense

of completeness, a (low-resolution) tomographic TPEF image of a rat retina is shown on the right panel of Fig. 4. Although the TPEF intensity depends on both, the retinal layer and the depth location, the images corresponding to the PRs provided the strongest signal and individual cells were clearly visible for both experimental conditions (Fig. 5).
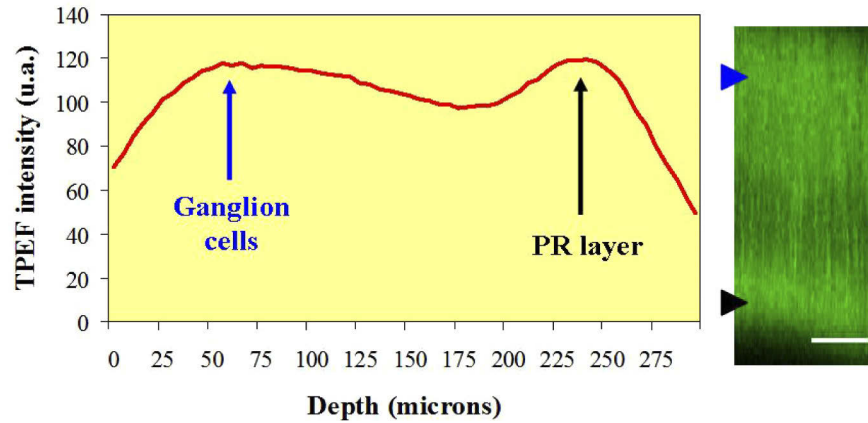

Fig. 4. TPEF intensity profile for a rat retina. This profile has been directly computed from the tomographic TPEF image shown on the right panel. Scale bar: 50 μm.
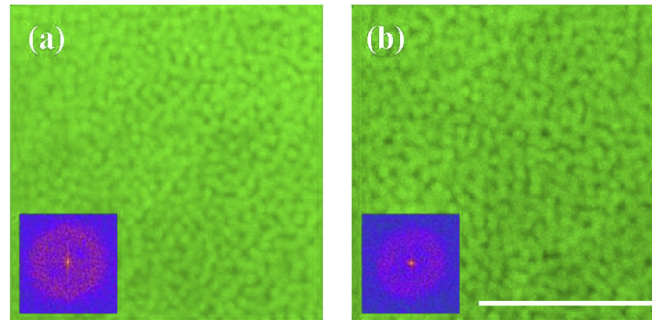

Fig. 5. Representative TPEF images of the PRs of a control (41481 cells/mm^2) (a) and a diabetic (35556 cells/mm^2) (b) rat retina for the same retinal eccentricity (location #1) and quadrant. Insets correspond to the Fourier transform image. Bar length: 50 μm.

As stated above, to evaluate the spatial distribution of PRs in the rat retina, local areas at different eccentricities have been examined. Figure 5 shows TPEF images for the same retinal location in a control and a diabetic retina. A direct qualitative comparison easily reveals that the number of PR is higher in the control retina (Fig. 5(a)). This is coherent with the radius of the ring appearing in the image corresponding to the Fourier transform of each PR mosaic (see Fig. 5 insets). For these representative images the density of PRs was 41481 cells/mm^2 for the control retina and reduced to 35556 cells/mm^2 for the pathological one.

For a control retina, Fig. 6 depicts the density of PRs as a function of the retinal eccentricity for two different quadrants (SN and ST). Density values increased from location #1 (close or near to the optic nerve head) to location #3 where a peak appears. Then, this decreases towards the retinal periphery reaching (at location #5) values close to those found at location #1. A paired t-test showed no significant differences (p=0.22) for the two series of density values shown in Fig. 6(a). The behavior was similar for the rest of retinal directions within this sample. Then,

for the rest of the work, the results for each location within a sample will be the averaged value among the four individual locations (one from each retinal quadrant, i.e. coloured rings in Fig. 2). This is showed in Fig. 6(b). Similar results were obtained for the rest of specimens involved in the present experiment, both control and pathological.
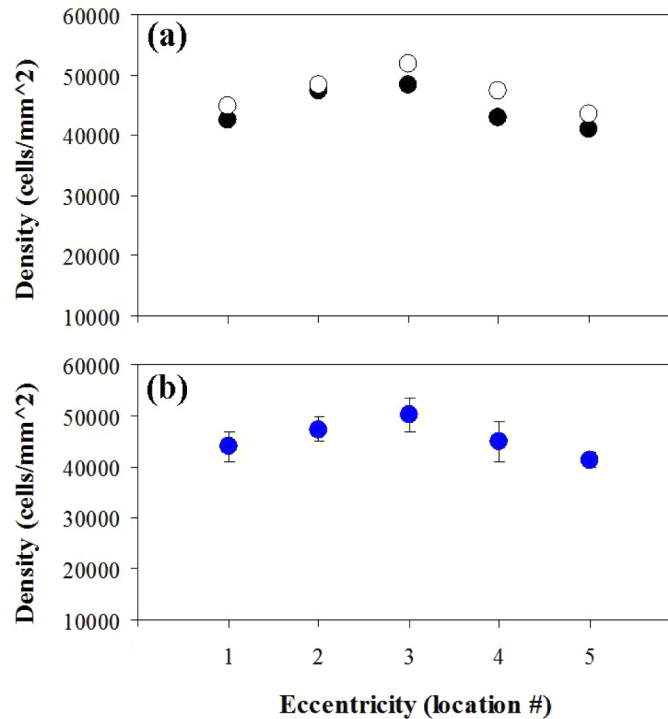

Fig. 6. (a) PR density (cells/mm^2) as a function of retinal eccentricity for two different retinal quadrants (SN and ST) in a control retina. (b) PR density values averaged across the four retinal quadrants of the same retina. Error bars indicate the standard deviation.

Figure 7 shows the density of PRs averaged across all specimens as a function of the retinal eccentricity in both control (blue) and diabetic (red) eyes. A visual inspection reveals that for every retinal location the values for diabetic retinas are well below those of control samples. In addition, differences between both data sets achieved statistical significance (Mann-Whitney U test; $p<0.0001$).

For the sense of completeness the ratio of PR density (control vs. diabetic) is depicted in Fig. 8. Although the values slightly depend on the location, overall PR density for control eyes was 31% higher than that of diabetic ones.

For a better description and understanding of the effects produced by the pathology on the PR distribution, a quantitative study based on Voronoi tessellations has been also carried out. As shown above, the density of PRs varies with eccentricity for both types of specimens. However, it is ignored whether the geometrical distribution also changes. In that sense, for two particular retinal locations (#1 and #3), Fig. 9 presents the frequency of appearance of the different Voronoi polygons as a function of the number of sides in a control sample.

It is observed that 6-sided polygons are predominant. This behavior was similar not only for the rest of retinal locations in control samples, but also for diabetic retinas. In that sense, a comparison of the PR mosaic packing geometry between control and pathological retinas
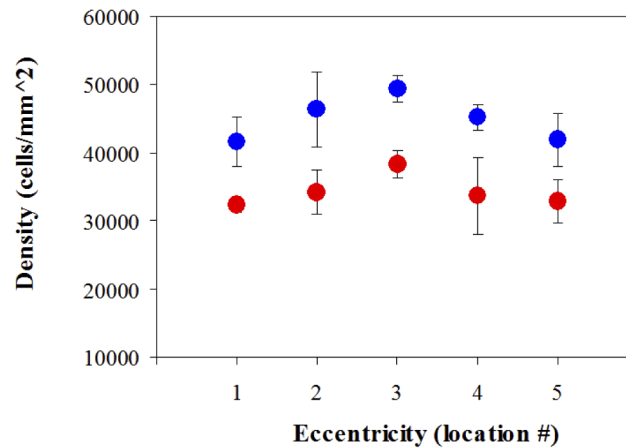
Fig. 7. Comparison of PR densities (cells/mm^2) as a function of the retinal eccentricity for diabetic (red symbols, N=8) and control (blue symbols, N=5) retinas. For every location each symbol represents the mean across all specimens within the corresponding experimental group.
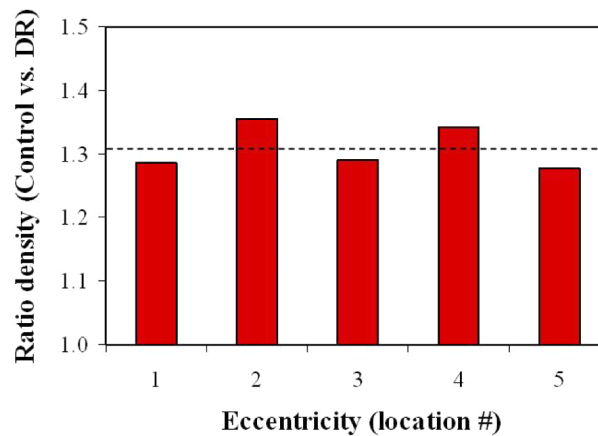

Fig. 8. Ratio of PR density (control vs. diabetic retinas) for all retinal eccentricities. Dashed line indicates the mean value.

is presented in Fig. 10. This depicts the variation in the number of Voronoi sides for both experimental conditions.

The highest fraction of polygons corresponded to hexagons, but there was a wide distribution of sizes ranging from 3- up to 9-sided. On average, across all retinas and locations, 35% of the PRs were hexagonally packed, and the prevalence was similar in pathological retinas (34%). The percentage for pentagons was 29 and 28% respectively, but decreased to 19 and 9% for 7- and 4-sided polygons for both types of retinas.

Figure 11 depicts the mean averaged distance (D_{MA}) as a function of the number of sides of the Voronoi polygons for both control and pathological retinas. Since it has been just showed that the polygon frequency distribution does not change with retinal eccentricity, the data have been also averaged across all locations for better comparisons. Differences between both groups of retinas were statistically significant (paired t-test, $p < 0.05$).
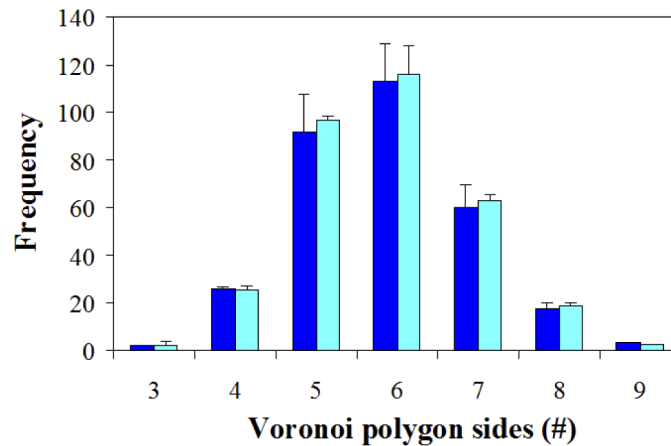
Fig. 9. Distribution of frequencies of Voronoi polygons for two representative retinal eccentricities in a control retina (location #1, light blue; location #3, marine blue). The specimen was randomly chosen. Each bar represents the mean value for a certain location across all four retinal quadrants. Note the predominance of the 6-sided polygons.
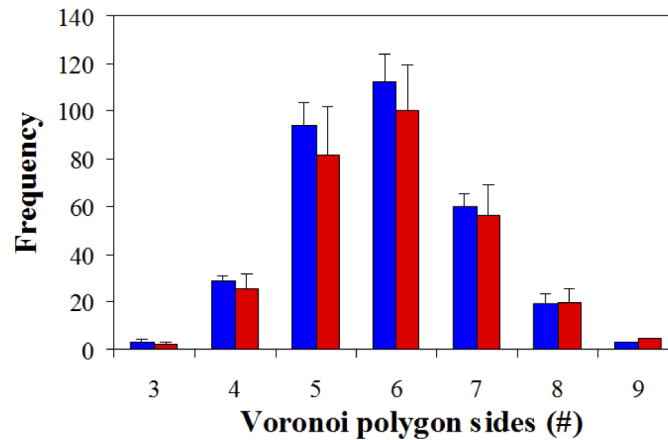

Fig. 10. Averaged frequency values of Voronoi polygons in control (blue) and diabetic (red) retinas. Each data is the mean across all locations and samples within the corresponding experimental group.

It is readily visible that, the PR spacing for 4-sided polygons is the longer one. For 5-, 6- and 7- sided ones, the distance among PRs is similar (and on average, 21% below that of 4-sided's). Moreover, independently of the number of sides, the parameter is always larger for diabetic samples (11% on average). As expected, this increase in D_{PR} might be a direct result of the reduction in the number of PRs associated with the DR.
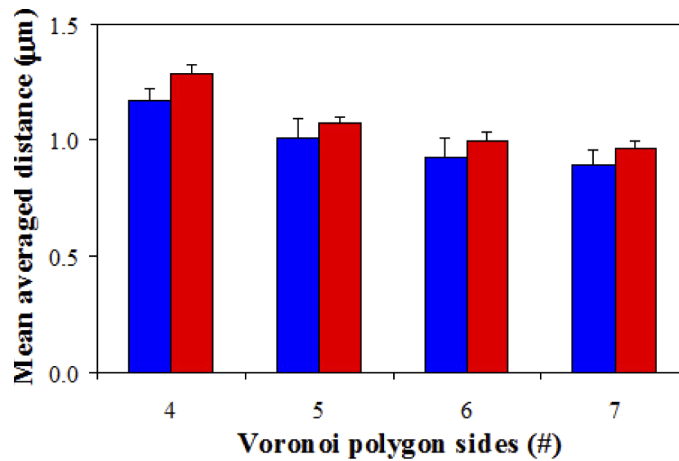
Fig. 11. Averaged inter-PR spacing (parameter D_{MA}) in control (blue, N=5) and DR (red, N=8) samples as a function of the number of sides of the Voronoi polygons. Each bar is the mean value across all retinal locations and samples. Error bars represent the standard deviation.

4. Discussion and conclusions

Biological structures often involve two-dimensional spatial arrangements. An accurate spatial characterization has important implications in both basic and applied investigations. The analysis of biological tissues requires quantitative measurements to explore cellular organization, and to understand, identify, and monitor changes during pathology development or healing processes.

Despite a number of authors have explored retinal changes in rat models under different pathological conditions, they always used markers to track retinal cells. To our knowledge there is not, to date, a study on density and geometrical distribution of PRs in diabetic rats using TPEF microscopy. In the present work, the distribution of PRs in non-stained pathological retinal tissues suffering from DR has been studied using TPEF images. In particular, PR densities have been mapped out and compared to those of healthy retinas. Moreover, geometrical cellular distribution has been quantified through Voronoi tessellations.

Unlike "regular" histological analyses where staining procedures are used, our imaging technique is able to visualize the PR mosaic without the need of markers. Thus, the TPEF detected signal was exclusively due to endogenous fluorescence [8,39], and individual cells are imaged with enough contrast to compute their density and spatial distribution.

Results herein reveal that, unlike other animal models or humans [9,41], the PR density in the control rat retina does not decrease with eccentricity. From 41500 cells/mm^2 at the central retina (location #1 is at 270 µm from the optic nerve head center) the values increase until reaching a maximum (49500 cells/mm^2), then a decrease takes place, presenting a value similar to that of the central part at the periphery (location #5). Furthermore, no statistically differences among the four retinal quadrants were found (as shown in Fig. 6). This behaviour of the PR density was similar in DR retinas. However at every retinal location, PR density was significantly reduced (31% on average) in these pathological specimens.

We have not found data on the spatial resolved PR density (cones and rods) in the rat retina to be compared. However, the patterns here found agree with the retinal ganglion cell and cone density maps in Sprague Dawley rats, where a maximum value at the middle peripheral retina was reported [36,42].

Our data are coherent with previous animal studies reporting that different retinal layers are influenced by the effects of diabetes. However, direct comparisons with our results are difficult not only because the experimental procedures and assessment methods noticeably differ, but also because different strains or genetic variations within the same animal model might lead to changes in the distribution of retinal cells [43].

Retinal modifications associated with DR include changes in the thickness and cellular density reduction, among others [32,44]. In diabetic Sprague-Dawley rats the thickness of the inner plexiform and the PR segment layers were significantly reduced [32]. The degeneration of rods/cones was found to be the most prominent pathological alteration in Sprague-Dawley and Wistar rats as measured one month [32] and 12 weeks after the onset of diabetes [33]. Retinal ganglion cell apoptosis (a decrease of about 27%) was also reported in a Wistar rat offspring model due to gestational diabetes [34]. Cell apoptosis due to diabetes has been shown not only in (Sprague–Dawley) rats [35] but also in mice (also induced by streptozotocin) [45]. The number of PRs also decreased in less-studied animal models such as Otsuka Long-Evans Tokushima Fatty (diabetes duration not reported) [46] and transgenic (mRen2)27 rats (3 weeks after the induction of diabetes) [47].

The maps of cellular distribution are associated with morphogenesis, mechanical stabilities and functional state. Then, Voronoi tessellations are appropriate tools to explore regularity cell arrangement. These add extra information to that provided just by measuring cellular density and help to better understand differences between control and pathological retinas.

As it can be seen in our datasets, the highest fraction of polygons in control retinas were hexagons. Previous Voronoi analyses have reported this geometry for cones in human and animal models [5,48–50]. Moreover, no changes in the percent of hexagonally packed cones with growth were reported in chickens [51].

However, in our animal model the presence of pentagonally packed PRs is also important. Let us remember that our procedure does not distinguish between cones and rods. Since the rat retina is ∼97% rod dominated [52], in practical terms, most of cells here imaged might be assumed to be rods. Moreover, to the best of our knowledge, there is a lack of studies on rod regularity in both control and DR rat models to be used as comparison.

It is interesting to point out that this trend of PRs to have six nearest neighbours is maintained in DR samples, despite the decrease in the local number total of Voronoi polygons (as expected from the reduction in density above reported). The reason for this is unclear but might be related to the time of diabetes onset, since longer periods might show more abrupt changes) [53].

The absence of changes in regularity in DR samples found in this work is in contrast with previous literature, although even those previous studies are not completely coincident. Lammer and co-workers found a correlation between cone packing disruption and DR severity, although the density of cones was within the limits of normal subjects [54]. On the contrary, a more recent study has reported cone density values (at 2° eccentricity) 20% lower in DR subjects compared to a control group. In addition, the mean percentage of cones with hexagonal Voronoi tiles also decreased [55].

From the Voronoi analyses, the parameter D_{MA} was also obtained. This has been reported to be very sensitive to changes in PR spacing [38]. Independently of the number of sides of the Voronoi polygons, the PR spacing increased in the samples with DR, what represents an expansion in cellular spacing. This effect agrees with the reduction in density above discussed.

To conclude, TPEF imaging microscopy has been successfully used to explore the changes in the PR mosaic of a diabetic rat model. This imaging technique enables single PR resolution and is an effective method of density assessment and geometrical packing analysis. PR density maps present a double-slope pattern with retinal eccentricity for both control and diseased specimens, although the latter showed significantly lower values. Voronoi tiling was used to quantitatively measure the spatial order of the retinas and to obtain information on cell spacing and packing

regularity. Control retinas showed a preference towards hexagonal packing and this regularity was not disrupted by diabetes even PR density being noticeable reduced.

TPEF microscopy is minimally invasive and provides high-resolution images, avoiding staining procedures. This study consolidates the procedure as being feasible for quantitatively explore healthy and pathological samples and detect abnormalities in the cellular arrangement. The implementation of this powerful tool in both research and clinical environments might complement and improve the results obtained with the existing instruments.

Funding

Acknowledgments

Disclosures

The authors declare no conflicts of interest.

References

1. M. Vidal-Sanz, M. Salinas-Navarro, F. M. Nadal-Nicolás, L. Alarcón-Martínez, F. J. Valiente-Soriano, J. Miralles de Imperial, M. Avilés-Trigueros, M. Agudo-Barriuso, and M. P. Villegas-Pérez, "Understanding glaucomatous damage: Anatomical and functional data from ocular hypertensive rodent retinas," Prog. Retinal Eye Res. **31**(1), 1–27 (2012).
2. Y. Qin, G. Xu, and W. Wang, "Dendritic abnormalities in retinal ganglion cells of three-month diabetic rats," Curr. Eye Res. **31**(11), 967–974 (2006).
3. M. E. Pennesi, M. Neuringer, and R. J. Courtney, "Animal models of age related macular degeneration," Mol. Aspects Med. **33**(4), 487–509 (2012).
4. J. Wallman and J. Winawer, "Homeostasis of eye growth and the question of myopia," Neuron **43**(4), 447–468 (2004).
5. J. I. W. Morgan, A. Dubra, R. Wolfe, W. H. Merigan, and D. R. Williams, "In vivo autofluorescence imaging of the human and macaque retinal pigment epithelial cell mosaic," Invest. Ophthalmol. Visual Sci. **50**(3), 1350–1359 (2009).
6. Y. F. Jian, J. Xu, M. A. Gradowski, S. Bonora, R. J. Zawadzki, and M. V. Sarunic, "Wavefront sensorless adaptive optics optical coherence tomography for in vivo retinal imaging in mice," Biomed. Opt. Express **5**(2), 547–559 (2014).
7. F. Helmchen and W. Denk, "Deep tissue two-photon microscopy," Nat. Methods **2**(12), 932–940 (2005).
8. Y. Imanishi, M. L. Batten, D. W. Piston, W. Baehr, and K. Palczewski, "Noninvasive two-photon imaging reveals retinyl ester storage structures in the eye," J. Cell Biol. **164**(3), 373–383 (2004).
9. J. M. Bueno, A. Giakoumaki, E. J. Gualda, F. Schaeffel, and P. Artal, "Analysis of the chicken retina with an adaptive optics multiphoton microscope," Biomed. Opt. Express **2**(6), 1637–1648 (2011).
10. J. M. Bueno, R. Palacios, A. Giakoumaki, E. J. Gualda, F. Schaeffel, and P. Artal, "Retinal cell imaging in myopic chickens using adaptive optics multiphoton microscopy," Biomed. Opt. Express **5**(3), 664–674 (2014).
11. B. G. Wang, A. Eitner, J. Lindenau, and K. J. Halbhuber, "High-resolution two-photon excitation microscopy of ocular tissues in porcine eye," Lasers Surg. Med. **40**(4), 247–256 (2008).
12. R.-W. Lu, Y.-C. Li, T. Ye, C. Strang, K. Keyser, C. A. Curcio, and X.-C. Yao, "Two-photon excited autofluorescence imaging of freshly isolated frog retinas," Biomed. Opt. Express **2**(6), 1494–1503 (2011).
13. H. Lim and J. Danias, "Label-free morphometry of retinal nerve fiber bundles by second-harmonic-generation microscopy," Opt. Lett. **37**(12), 2316–2318 (2012).
14. A. Batista, H. G. Breunig, A. König, A. M. Morgado, and K. König, "Assessment of the metabolism and morphology of the porcine cornea, lens, and retina by two-photon imaging," J. Biophotonics **11**(7), e201700324 (2018).
15. S. He, C. Ye, Q. Sun, C. K. S. Leung, and J. Y. Qu, "Label-free nonlinear optical imaging of mouse retina," Biomed. Opt. Express **6**(3), 1055–1066 (2015).
16. J. J. Hunter, B. Masella, A. Dubra, R. Sharma, L. Yin, W. H. Merigan, G. Palczewska, K. Palczewski, and D. R. Williams, "Images of photoreceptors in living primate eyes using adaptive optics two-photon ophthalmoscopy," Biomed. Opt. Express **2**(1), 139–148 (2011).
17. R. Sharma, C. Schwarz, J. J. Hunter, G. Palczewska, K. Palczewski, and D. R. Williams, "Formation and clearance of all-trans-retinol in rods investigated in the living primate eye with two-photon ophthalmoscopy," Invest. Ophthalmol. Visual Sci. **58**(1), 604–613 (2017).

18. R. Sharma, L. Yin, Y. Geng, W. H. Merigan, G. Palczewska, K. Palczewski, D. R. Williams, and J. J. Hunter, "In vivo two-photon Imaging of the mouse retina," Biomed. Opt. Express **4**(8), 1285–1293 (2013).

19. J. J. Mancuso, A. M. Larson, T. G. Wensel, and P. Saggau, "Multiphoton adaptation of a commercial low-cost confocal microscope for live tissue imaging," J. Biomed. Opt. **14**(3), 034048 (2009).

20. E. J. Gualda, J. M. Bueno, and P. Artal, "Wavefront optimized nonlinear microscopy of ex vivo human retinas," J. Biomed. Opt. **15**(2), 026007 (2010).

21. M. Han, A. Bindewald-Wittich, F. G. Holz, G. Giese, M. H. Niemz, S. Snyder, H. Sun, J. Y. Yu, M. Agopov, O. La Schiazza, and J. F. Bille, "Two-photon excited autofluorescence imaging of human retinal pigment epithelial cells," J. Biomed. Opt. **11**(1), 010501 (2006).

22. M. Han, G. Giese, S. Schmitz-Valckenberg, A. Bindewald-Wittich, F. G. Holz, J. Y. Yu, J. F. Bille, and M. H. Niemz, "Age-related structural abnormalities in the human retina-choroid complex revealed by two-photon excited autofluorescence imaging," J. Biomed. Opt. **12**(2), 024012 (2007).

23. O. La Schiazza and J. J. Bille, "High-speed two-photon excited autofluorescence imaging of *ex vivo* human retinal pigment epithelial cells toward age-related macular degeneration diagnostic," J. Biomed. Opt. **13**(6), 064008 (2008).

24. R. N. Frank, "Diabetic retinopathy," N. Engl. J. Med. **350**(1), 48–58 (2004).

25. C. M. Morello, "Etiology and natural history of diabetic retinopathy, an overview," Am. J. Health-Syst. Pharm. **64**(17_Supplement_12), S3–S7 (2007).

26. T. Y. Wong, R. Klein, F. M. Islam, M. F. Cotch, A. R. Folsom, B. E. Klein, A. R. Sharrett, and S. Shea, "Diabetic retinopathy in a multi-ethnic cohort in the United States," Am. J. Ophthalmol. **141**(3), 446–455.e1 (2006).

27. T. W. Gardner, D. A. Antonetti, A. J. Barber, K. F. LaNoue, and S. W. Levison, "Diabetic retinopathy, more than meets the eye," Surv. Ophthalmol. **47**(Suppl. 2), S253–S262 (2002).

28. Y. Alvarez, K. Chen, A. L. Reynolds, N. Waghorne, J. J. O'Connor, and B. N. Kennedy, ", "Predominant cone photoreceptor dysfunction in a hyperglycaemic model of non-proliferative diabetic retinopathy," Dis. Models Mech. **3**(3-4), 236–245 (2010).

29. Y. Du, A. Veenstra, K. Palczewski, and T. S. Kern, "Photoreceptor cells are major contributors to diabetes-induced oxidative stress and local inflammation in the retina," Proc. Natl. Acad. Sci. U. S. A. **110**(41), 16586–16591 (2013).

30. T. S. Kern and B. A. Berkowitz, "Photoreceptors in diabetic retinopathy," J. Diabetes Invest. **6**(4), 371–380 (2015).

31. T. S. Kern, "Do photoreceptor cells cause the development of retinal vascular disease?" Vision Res. **139**, 65–71 (2017).

32. Y. Aizu, K. Oyanagi, J. Hu, and H. Nakagawa, "Degeneration of retinal neuronal processes and pigment epithelium in the early stage of the streptozotocin-diabetic rats," Neuropathology **22**(3), 161–170 (2002).

33. A. Énzsoly, A. Szabó, O. Kántor, C. Dávid, P. Szalay, K Szabó, A. Szél, J. Németh, and A. Lukáts, "Pathologic alterations of the outer retina in streptozotocin-induced diabetes," Invest. Ophthalmol. Visual Sci. **55**(6), 3686–3699 (2014).

34. S. Najafdari, N. Rezaei, M. M. Shafaroodi, S. Ghafari, and M. J. Golalipour, "Ganglionic cells apoptosis in retinal layer of rat offspring due to gestational diabetes," Int. J. Morphol. **32**(4), 1131–1135 (2014).

35. S. H. Park, J. W. Park, S. J. Park, K. Y. Kim, J. W. Chung, M. H. Chun, and S. J. Oh, "Apoptotic death of photoreceptors in the streptozotocin-induced diabetic rat retina," Diabetologia **46**(9), 1260–1268 (2003).

36. M. Salinas-Navarro, S. Mayor-Torroglosa, M. Jiménez-López, M. Avilés-Trigueros, T. M. Holmes, R. D. Lund, M. P. Villegas-Pérez, and M. Vidal-Sanz, "A computerized analysis of the entire retinal ganglion cell population and its spatial distribution in adult rats," Vision Res. **49**(1), 115–126 (2009).

37. A. Okabe, B. Boots, K. Sugihara, and S. N. Chiu, *Spatial tessellations: Concepts and applications of Voronoi diagrams* (Wiley, New York, 2000).

38. J. Sudbø, R. Marcelponil, and A. Reith, "New algorithms based on the Voronoi diagram applied in a pilot study on normal mucosa and carcinomas," Anal. Cell. Pathol. **21**(2), 71–86 (2000).

39. Y. Imanishi, K. H. Lodowski, and Y. Koutalos, "Two-photon microscopy: shedding light on the chemistry of vision," Biochemistry **46**(34), 9674–9684 (2007).

40. J. M. Bueno, R. Palacios, A. Pennos, and P. Artal, "Second-harmonic generation microscopy of photocurable polymer intrastromal implants in ex-vivo corneas," Biomed. Opt. Express **6**(6), 2211–2219 (2015).

41. C. A. Curcio and K. R. Sloan, "Packing geometry of human cone photoreceptors - variation with eccentricity and evidence for local anisotropy," Vis. Neurosci. **9**(2), 169–180 (1992).

42. A. Ortín-Martínez, M. Salinas-Navarro, F. M. Nadal-Nicolás, M. Jiménez-López, F. J. Valiente-Soriano, D. García-Ayuso, J. M. Bernal-Garro, M. Avilés-Trigueros, M. Agudo-Barriuso, M. P. Villegas-Pérez, and M. Vidal-Sanz, "Laser-induced ocular hypertension in adult rats does not affect non-RGC neurons in the ganglion cell layer but results in protracted severe loss of cone-photoreceptors," Exp. Eye Res. **132**, 17–33 (2015).

43. A. S. Jelcick, Y. Yuan, B. D. Leehy, L. C. Cox, A. C. Silveira, F. Qiu, S. Schenk, A. J. Sachs, M. A. Morrison, A. M. Nystuen, M. M. DeAngelis, and N. B. Haider, "Genetic variations strongly influence phenotypic outcome in the mouse retina," PLoS One **6**(7), e21858 (2011).

44. Y. Revsin, F. Saravia, P. Roig, A. Lima, E. R. de Kloet, F. Homo-Delarche, and A. F. De Nicola, "Neuronal and asteroglial alteration in the hippocampus of a mouse model for type 1 diabetes," Brain Res. **1038**(1), 22–31 (2005).

45. P. M. Martin, P. Roon, T. K. Van Ells, V. Ganapathy, and S. B. Smith, "Death of retinal neurons in streptozotocin-induced diabetic mice," Invest. Ophthalmol. Visual Sci. **45**(9), 3330–3336 (2004).

46. Z. Y. Lu, I. A. Bhutto, and T. Amemiya, "Retinal changes in Otsuka long-evans Tokushima Fatty rats (spontaneously diabetic rat)–possibility of a new experimental model for diabetic retinopathy," Jpn. J. Ophthalmol. **47**(1), 28–35 (2003).

47. W. W. Batenburg, A. Verma, Y. Wang, P. Zhu, M. van den Heuvel, R. van Veghel, A. H. J. Danser, and Q. Li, "Combined rennin inhibition/(Pro)Renin receptor blockade in diabetic retinopathy - A study in transgenic (mREN2)27 rats," PLoS One **9**(6), e100954 (2014).

48. K. Y. Li and A. Roorda, "Automated identification of cone photoreceptors in adaptive optics retinal images," J. Opt. Soc. Am. A **24**(5), 1358–1363 (2007).

49. Y. Kram, S. Manty, and J. Corbo, "Avian cone photoreceptors tile the retina as five independent, self-organizing mosaics," PLoS One **5**(2), e8992 (2010).

50. K. Headington, S. S. Choi, D. Nickla, and N. Doble, "Single cell imaging of the chick retina with adaptive optics," Curr. Eye Res. **36**(10), 947–957 (2011).

51. M. L. Kisilak, K. Bunghardt, J. J. Hunter, E. L. Irving, and M. C. Campbell, "Longitudinal in vivo imaging of cones in the alert chicken," Optom. Vis Sci. **89**(5), 644–651 (2012).

52. A. Cunea and G. Jeffery, "The ageing photoreceptor," Vis. Neurosci. **24**(2), 151–155 (2007).

53. C. Y. Gong, B. Lu, Q. W. Hu, and L. L. Ji, "Streptozotocin induced diabetic retinopathy in rat and the expression of vascular endothelial growth factor and its receptor," Int. J. Ophthalmol. **6**(5), 573–577 (2013).

54. J. Lammer, S. G. Prager, M. C. Cheney, A. Ahmed, S. H. Radwan, S. A. Burns, P. S. Silva, and J. K. Sun, "Cone photoreceptor irregularity on adaptive optics scanning laser ophthalmoscopy correlates with severity of diabetic retinopathy and macular edema," Invest. Ophthalmol. Vis. Sci. **57**(15), 6624–6632 (2016).

55. A. Zaleska-Żmijewska, Z. M. Wawrzyniak, A. Dąbrowska, and J. P. Szaflik, "Adaptive Optics (rtx1) High-Resolution Imaging of Photoreceptors and Retinal Arteries in Patients with Diabetic Retinopathy," J. Diabetes Res. **2019**, 9548324 (2019).